PAPER

Kinetic insights into thrust generation and electron transport in a magnetic nozzle

To cite this article: Yuan Hu *et al* 2021 *Plasma Sources Sci. Technol.* **30** 075006

IOP Publishing Plasma Sources Science and Technology
Plasma Sources Sci. Technol. **30** (2021) 075006 (12pp) https://doi.org/10.1088/1361-6595/ac0a48

Kinetic insights into thrust generation and electron transport in a magnetic nozzle

Yuan Hu[1], Zilin Huang[1,2], Yong Cao[3] and Quanhua Sun[1,2,*]

[1] State Key Laboratory of High Temperature Gas Dynamics, Institute of Mechanics, Chinese Academy of Sciences, Beijing 100190, People's Republic of China
[2] School of Engineering Science, University of Chinese Academy of Sciences, Beijing 100049, People's Republic of China
[3] Department of Mechanical Engineering & Automation, Harbin Institute of Technology (Shenzhen), Shenzhen, Guangdong 518055, People's Republic of China

E-mail: qsun@imech.ac.cn

Received 25 February 2021, revised 14 May 2021
Accepted for publication 10 June 2021
Published 5 July 2021

Abstract

Axisymmetric fully kinetic particle-in-cell simulations are carried out to study the expansion of plasma in a propulsive magnetic nozzle (MN). The simulation results reveal that the MN can boost the total thrust while the on-axis ion acceleration may be suppressed, demonstrating the necessity of including two-dimensional effects if the propulsive performance is the primary concern. The magnetic thrust resulting from the interaction of azimuthal electric current with the applied magnetic field is identified as the only source of enhancing the plasma plume thrust. It is found that the role of electron transport, in connection with the stress tensor, cannot be neglected in fluid modeling. The electron transport effects will induce a paramagnetic drift current and thus undermine the propulsive performance of MN.

Keywords: magnetic nozzle, electron transport, thrust generation, particle-in-cell

(Some figures may appear in colour only in the online journal)

1. Introduction

The expanding magnetic field used to confine hot plasmas radially and to convert their thermal energy into axial kinetic energy through expansion, in analogy to the conventional Laval nozzle's operation on neutral gases, are named magnetic Laval nozzle or magnetic nozzle (MN) for simplicity [1, 2]. MNs are being considered as a promising concept to boost the propulsive performance of various electric propulsion (EP) devices such as the helicon plasma thruster (HPT) [3–5], the electron cyclotron resonance thruster (ECRT) [6, 7], the applied field magnetoplasma dynamic thruster (AFMPDT) [8], the variable specific impulse magnetoplasma rocket [9, 10], etc. Despite the similarity in the purpose of converting the random internal energy into the directed kinetic energy, MNs differ significantly from the solid nozzles in the mechanisms of plasma acceleration and thrust generation, which are far more complex in MNs attributed to the long range electromagnetic forces as well as nonequilibrium thermodynamics at play.

Andersen *et al* [1, 2] investigated the acceleration of plasma in an MN by solving a set of governing equations similar to the one used for the conventional Laval nozzle, except that the adiabatic assumption usually made in the neutral gas expansion was replaced by with the isothermal approximation in the plasma expansion. In this model, the plasma acceleration is completed through the ambipolar electric field. Since then, much effort has been made to understand the ambipolar acceleration mechanism in MNs [11–13]. The ambipolar acceleration can be regarded as an electric field acceleration (EFA) mechanism. Another type of EFA is the double layer (DL) acceleration, which is usually seen in the MN of HPT [3, 14–17]. Despite occurring in a much smaller region for DLs, the total potential drop across both ambipolar field and DL is shown to be comparable [18]. Moreover, it has been demonstrated that the electric field associated with DL does

* Author to whom any correspondence should be addressed.

not impart net force and momentum, and thereby does not help thrust enhancement [18–20].

It is believed that, in order for plasmas in MNs to deliver momentum, the interaction of the applied magnetic field with the plasma through the Lorentz force must come into play. Ahedo and Merino solved an axisymmetric two-fluid model to investigate the plasma acceleration and thrust enhancement in MNs [21]. It was found that, besides the ambipolar acceleration, the interaction of the Hall (electron azimuthal) current with the applied magnetic field or the Lorentz force could produce additional acceleration. More importantly, it is the Hall acceleration mechanism that is responsible for imparting momentum and creating additional (magnetic) thrust. Later on, the momentum of plasma transmitted to the expanding magnetic field was directly measured and compared with the result based on a two-fluid theory, confirming that magnetic thrust is produced by the Hall acceleration mechanism [22–24]. The electron azimuthal currents in MNs were also directly measured and recognized as the sum of the diamagnetic and $\mathbf{E}\times\mathbf{B}$ drift currents [25].

While great successes have been achieved in understanding the mechanisms underlying the plasma acceleration and thrust generation in MNs, there are some issues deserving further discussions.

The ideal fluid model was adopted by all previous fluid-based analyses of MN plasma flows. Many studies further used the polytropic law of equation (1) for electrons to close the governing equations to be solved at the momentum level [21, 23, 26].

$$\frac{p_{\mathrm{e}}}{n_{\mathrm{e}}^{\gamma_{\mathrm{e}}}}=\text{constant},\quad \text{or}\quad \frac{T_{\mathrm{e}}}{n_{\mathrm{e}}^{\gamma_{\mathrm{e}}-1}}=\text{constant}. \tag{1}$$

Note that $\gamma_{\mathrm{e}}=1$ and $5/3$ correspond to the isothermal and adiabatic conditions, respectively. The choice of γ_{e} was somewhat arbitrary in the literature, and the isothermal condition was mostly used [21, 23]. However, the values of γ_{e} have been proved to have significant influence on the prediction of plasma properties in MNs [26].

Many experiments were carried out to study the electron thermodynamic processes in MNs. The measured γ_{e} was reported to vary most commonly between 1.1 and 1.25 [7, 27, 28]. Some recent experiments able to distinguish between the freely expanding and trapped electrons suggested that the former population tended to be adiabatic (γ_{e} close to 5/3) while the latter one was nearly isothermal ($\gamma_{\mathrm{e}}\simeq 1$) [29–31]. Despite the inconsistency of the measured γ_{e} among different groups, which indicates the electron thermodynamics might be device-dependent, these measurements were carried out along the symmetric axis while the plasma flows in MNs have been proved to show obvious two-dimensional (2D) features. Consequently, the experimentally determined γ_{e} may not be ready for use in the popular fluid models.

The electron thermodynamics is complicated because the plasmas in MNs are usually collisionless, resulting in the deviations of electrons from local thermodynamic equilibrium. To handle this issue properly, the kinetic methods are needed. The one-dimensional (1D) paraxial kinetic models were developed to analyze the electron thermodynamics and its effects on the plasma expansion dynamics in MNs [32, 33]. In essence, the kinetic models can treat the heat transfer process self-consistently. The paraxial kinetic studies found that the heat fluxes in MN plasmas manifested anisotropic and non-Fourier features.

Compared to the thermodynamics, the role of electron transport in the fluid treatment of MN plasma expansion was much less addressed. The ideal fluid model, from which the stress tensor terms are absent, ignores all transport effects. In fact, the nonlocal electron behaviors have been observed in MNs or similar devices where the electrons are collisionless and confined by magnetic fields [34–36], implying that the electron transport effects may be crucial.

Computationally demanding fully kinetic simulations are needed to consistently treat the thermodynamic and transport processes of electrons in 2D and 3D problems. However, the amount of such works are limited. Rao and Singh [17, 37] conducted 2D fully kinetic particle-in-cell (PIC) simulations and recovered the 2D DL structure similar to the experimental observation in reference [15]. A recent work by Chen *et al* [38] revealed the lateral potential barrier structure near the MN throat usually observed when the ion temperature is high [26, 39]. It was believed that the potential barrier served to confine ions and create thrust for the MN. While these fully kinetic simulations have provided great insight into the plasma acceleration and thrust generation in MNs, they were performed in unrealistic 2D planar geometries. The simulation domain sizes were also very limited such that the boundary condition might cause undesired pollutions on the results [5]. Recently, a 2D cylindrical (axisymmetric) full PIC model was applied to study the acceleration of plasma in the plume of a micro-cathode vacuum arc thruster with an MN-type acceleration stage [40]. However, the study was still limited by the small simulation domain used.

In this paper, we are going to perform large scale 2D3V axisymmetric fully kinetic PIC simulations on the expansion of plasma plume in an MN. We consider the HPT- or ECRT-type plume, where the electrons are thermal while the ions are cold. The focus is to provide a fully kinetic insight into the mechanism of thrust generation in MNs, with an emphasis on the role of electron transport. The rest of this paper is organized as follows. Section 2 describes the physical and numerical models. Section 3 presents the results obtained by our high fidelity fully kinetic simulations. Section 4 discusses the mechanism of magnetic thrust generation from the fully kinetic point of view. We investigate the effects of electron transport on the accuracy of fluid modeling and its role in magnetic thrust production in section 5. We conclude this study with section 6.

2. Physical and numerical models

Figure 1 shows the schematic of the simulation setup. The plasma plume is considered to be emitted from the source located at $(z,r)=(0,0\sim R_0)$, where R_0 is source radius. The magnetic field forming the MN is created by a model coil with the radius $R_{\mathrm{coil}}=2R_0$, similar to the configuration in reference [28]. MRFL is an abbreviation of the

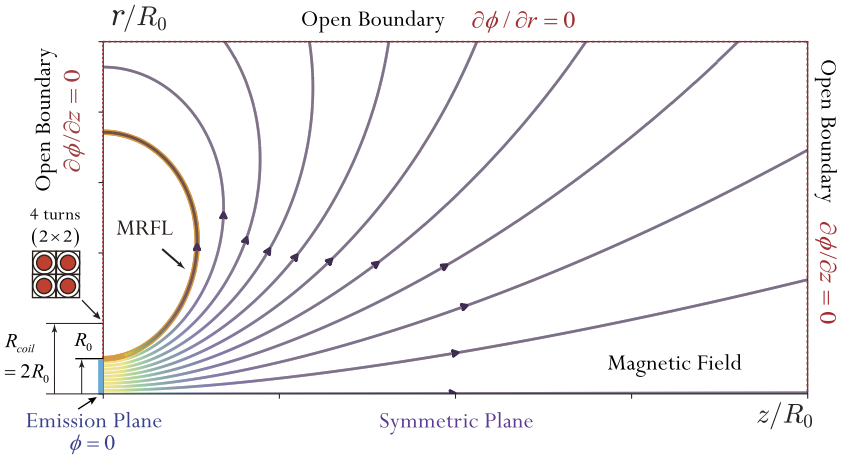

Figure 1. Schematic of applied magnetic field and simulation setup.

most radial field line escaping the plasma source named in reference [41].

The plasma induced magnetic field is typically small enough to be neglected in the MNs associated with HPT or ECRT so the electrostatic full PIC model is used. The particle position $\mathbf{x}$ and velocity $\mathbf{v}$, the number densities of ion n_i and electron n_e, and the electric potential Φ are solved self-consistently from Newton's equation of motion and Poisson's equation in a cylindrical coordinate system

$$\mathbf{v} = \frac{\mathrm{d}\mathbf{x}}{\mathrm{d}t}, \qquad \frac{\mathrm{d}}{\mathrm{d}t}(m\mathbf{v}) = \mathbf{F}, \quad \mathbf{F} = q\left(-\nabla\Phi + \mathbf{v}\times\mathbf{B}\right), \quad (2)$$

$$-\nabla^2\Phi = \frac{e}{\epsilon_0}\left(n_\mathrm{i} - n_\mathrm{e}\right), \quad (3)$$

where $q = \pm e$ and m denote the particle charge and mass, respectively, e is the elementary charge, and ϵ_0 is the vacuum permittivity.

The current-free and far field boundary conditions are implemented in the same way as reference [42]. The simulations are carried out in a dimensionless form. The number density and temperature for the ions and electrons are chosen to be: $\tilde{n}_\mathrm{e} = n_\mathrm{e}/n_0 = 1$, $\tilde{n}_\mathrm{i} = n_\mathrm{i}/n_0 = 1$, $\tilde{T}_\mathrm{e} = T_\mathrm{e}/T_0 = 1$, $\tilde{T}_\mathrm{i} = T_\mathrm{i}/T_0 = 0.025$. The bulk velocity of plasma (v_0) at source exit is chosen such that the Mach number $M = v_0/C_{s0} = v_0/\sqrt{k_\mathrm{b}T_0/m_\mathrm{i}} = 1$, where k_b denotes the Boltzmann constant. The subscript '0' in the expressions above corresponds to the physical quantities of reference. The value of $\tilde{T}_\mathrm{i} = 0.025$ is typical for HPT devices [17]. We have used the proton-to-electron mass ratio ($m_\mathrm{i}/m_\mathrm{e} = 1836$), same as our previous work about the plasma expansion in the absence of MN [42]. The ion-to-electron mass ratio mainly affects the electron thermodynamics in the context of plasma expansion. It has been demonstrated that the difference of mass between argon and proton cannot cause noticeable errors to the plasma expansion dynamics [43]. This is also a common ion mass used in recent 2D planar PIC simulations of plasma expansion in the MN [17, 38]. The magnitude of magnetic field is controlled by the normalized ion cyclotron frequency $\hat{\Omega}_{\mathrm{i}0} = R_0 eB_0/(m_\mathrm{i}C_{s0})$ with $B_0 = B(z = 0, r = 0)$, following the notation of Ahedo and Merino [21]. In this paper, the cases with $\hat{\Omega}_{\mathrm{i}0} = 0$ and 0.2 are considered. The former one represents the geometric expansion of our recent work [42] and the latter one is the MN plasma expansion. We choose $\hat{\Omega}_{\mathrm{i}0} = 0.2$ because it is a representative value for most MNs associated with HPT and ECRT [15, 21, 28, 29]. The source radius is set as $R_0 = 10\lambda_{\mathrm{D}0}$, proved to be a great balance between the physical accuracy and computational cost [17, 38, 42]. The electron cyclotron radius corresponds to $r_{\mathrm{ce}} \simeq \lambda_{\mathrm{D}0}$.

The mesh resolution used is $\Delta z = \Delta r = \lambda_{\mathrm{D}0}$ and the simulation time step is $\Delta t = 0.1\omega_{\mathrm{pe}0}^{-1}$, where $\lambda_{\mathrm{D}0} = \sqrt{\epsilon_0 k_\mathrm{b}T_0/n_0e^2}$ and $\omega_{\mathrm{pe}0} = \sqrt{n_0e^2/\epsilon_0 m_\mathrm{e}}$ are the Debye length and electron plasma frequency computed according to source plasma parameters, respectively. The size of the simulation domain $(z/\lambda_{\mathrm{D}0}, r/\lambda_{\mathrm{D}0})$ used is $(0 \sim 2048, 0 \sim 2048)$, about $205R_0$ in each direction. A uniform particle weight is used to avoid the errors which will be introduced by particle splitting and merging in a non-uniform particle weight scheme. The total number of macro-particles at the completion of a simulation run is about 200 million. The simulations are first run for $t\omega_{\mathrm{pi}} = 400$, corresponding to over 5 ion transient periods, to guarantee the steady state and then diagnostics for interested physical quantities are performed. The devised setup and parameters have been demonstrated to be appropriate for steady collisionless plasma plume simulations with the focus on accurate electron kinetic behaviors by our previous work [42]. In particular, the size of simulation domain in each direction in this work is an order of magnitude larger than the reported full PIC simulations [17, 37, 38, 40]. As pointed out in reference [5], the appropriate definition of downstream boundary condition is still a challenging problem because of non-local response of collisionless electrons. While we have used the state-of-art strategy proposed by Li *et al* [44], a large domain size is still recommended in order to reduce the undesired pollutions on the simulation results if the computational cost is affordable.

3. Simulation results

Figure 2 shows the 2D contours of various plasma properties, including the ion number density, electron number density,

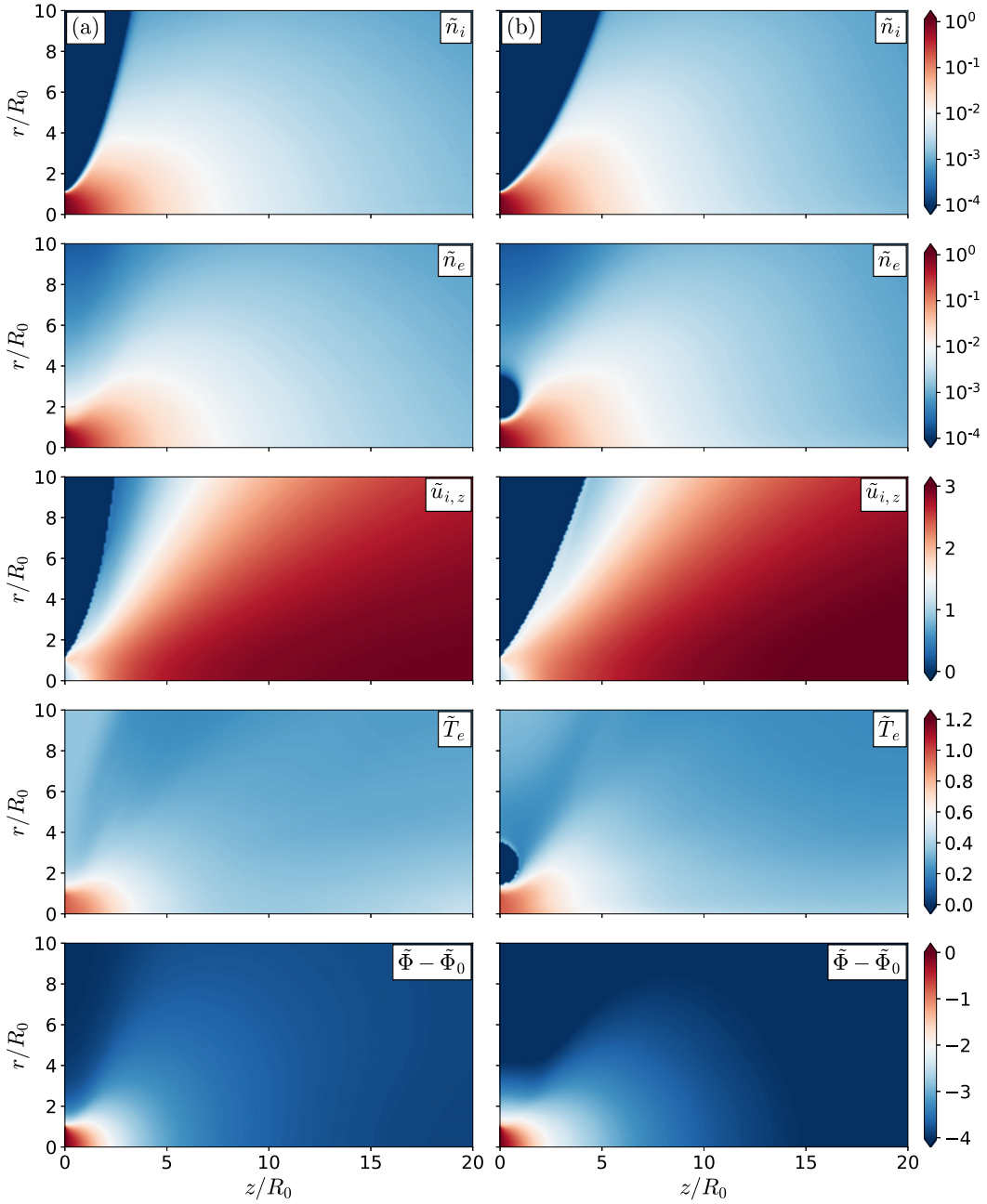

Figure 2. Plasma fields: (a) without versus (b) with applied magnetic field.

axial ion velocity, electron temperature, and potential drop. The cases without and with the applied magnetic field are presented for comparison. Note that to control the numerical noise, the plasma properties in the near vacuum region ($\tilde{n} < 1 \times 10^{-4}$) are set to the minimum values given in the plot, except for the electric potential.

In the absence of magnetic field, the plasma plume follows a typical geometric expansion driven by the ambipolar electric field [42–44]. There is a clear boundary between the ion plasma and vacuum while no such a boundary is observed for the electron because it is thermal and much more mobile. The magnetic field helps to confine the plasma. This is evidenced by the lower divergence of ion plume (see $\tilde{n}_\mathrm{i}$ for example) and the electron void near the outer region of throat radially. It is also observed that, in the presence of magnetic field, the potential drop of near plume ($z < 10R_0$ if we focus on the axis) is slightly smaller, while the potential drop of far plume is larger. In fact, the strength of magnetic field in our simulation is too small to alter the ion trajectories. Consequently, we can conclude that the presence of magnetic field helps to confine the electrons and thereby changes the potential profile, which in turn leads to the reduction of divergence of ion plume.

Figure 3 shows the 1D profiles of near plume along the z-axis for a more careful examination of the effects of magnetic field on interested plasma properties. It is worth mentioning that the electron temperature is evaluated by computing the second moment of velocity given in equation (4) in the particle

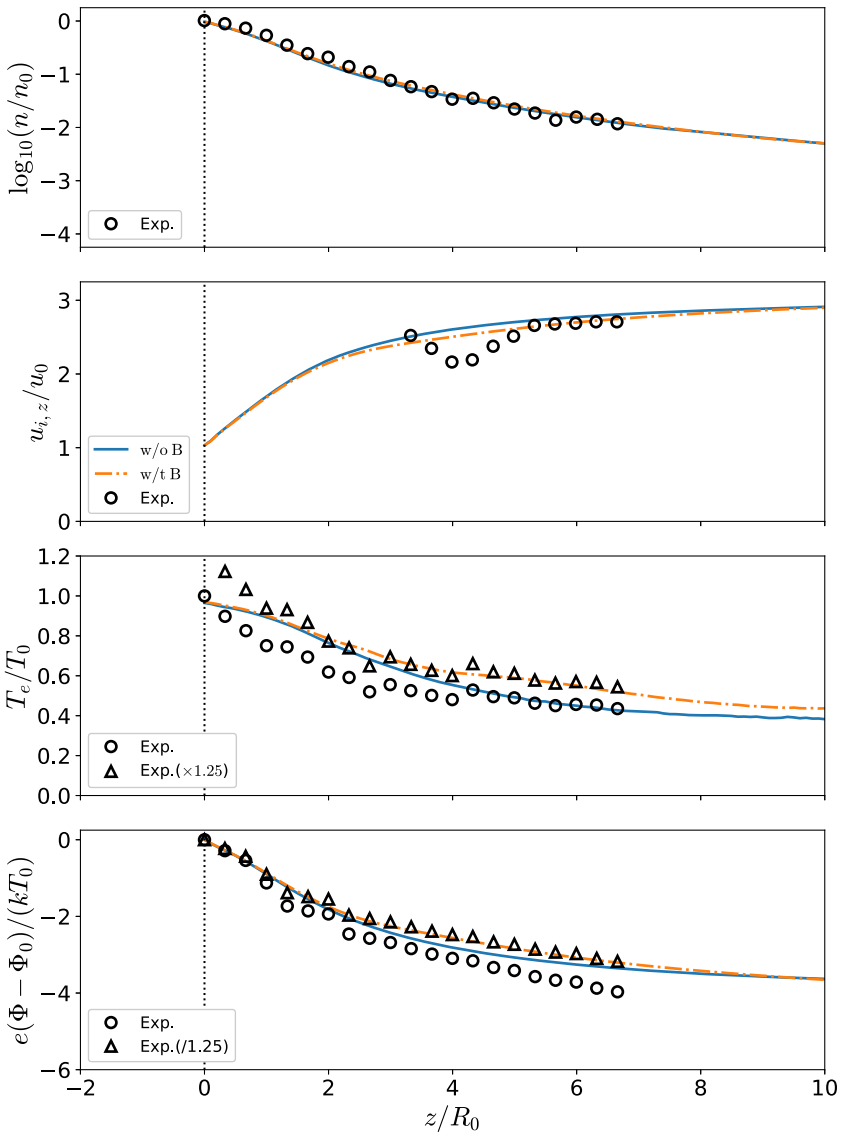

Figure 3. Plasma properties along z-axis from PIC simulations without and with applied magnetic field. The experiment data from reference [28] are presented for comparison.

manner.

$$T_\mathrm{e} \equiv \frac{1}{3n_\mathrm{e}k_\mathrm{b}} \int m_\mathrm{e} |(\mathbf{v}-\mathbf{u}_\mathrm{e})|^2 f_\mathrm{e}(\mathbf{x},\mathbf{v})\,\mathrm{d}^3\mathbf{v}. \tag{4}$$

This equation gives the average of the components in different directions so it implicitly includes anisotropic effects if the axial, radial and azimuthal components of temperature are different. The MN experiment data from reference [28] are also presented. Our results of plasma density and ion velocity agree quite well with the experiment data. There are observable discrepancies in electron temperature and potential profiles between our simulation and the experiment. However, the agreements between the simulation and experimental data are considerable improved if we multiply the measured electron temperature by a factor of 1.25 while divide the potential drop by the same factor. The differences between the simulation and experiment might result from the reduced length scale in the simulations. The comparisons nevertheless show the most important physical processes are consistent between the reduced scale simulation and experiment. It can be found from figure 3 that the presence of magnetic field slightly increases the plasma density and electron temperature, arising from the effect of magnetic confinement. The on-axis velocity of ions in the presence of MN is observed to be smaller than that in the absence of MN until $z \simeq 10R_0$. The crossing point on ion velocity profile is consistent with the result on the potential profile.

The $\log_{10}T_\mathrm{e}$ versus $\log_{10}n_\mathrm{e}$ relation is plotted in figure 4. The linear relationship between these datasets demonstrates the electrons in both magnetically and geometrically expanding plasmas follow the polytropic law. The linear regression of the data yields $\gamma_\mathrm{e} \approx 1.16$ and 1.23 with and without the applied magnetic field, respectively. The experimentally measured γ_e for MN plasmas is reported to vary most commonly between 1.1 and 1.25 [7, 27, 28]. Moreover, it is found that γ_e for unmagnetized plasma expansion also lies in the range of

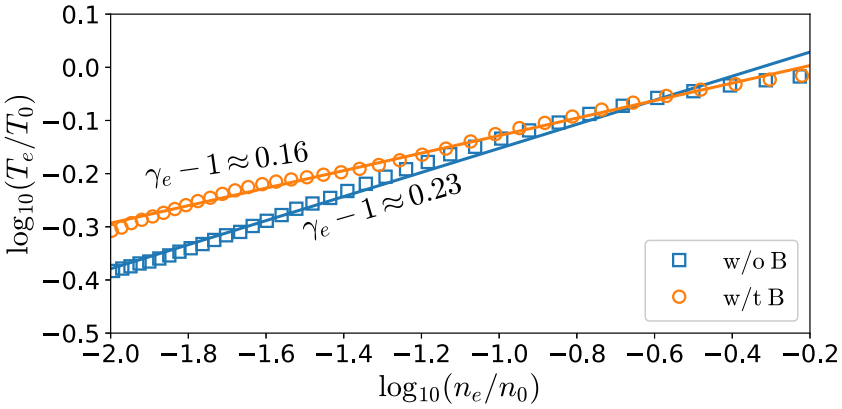

Figure 4. $\log_{10}(T_e)$ versus $\log_{10}(n_e)$ based on PIC results along z-axis from PIC simulations without and with applied magnetic field. The best fitting values for γ_e are also given.

1.1 to 1.3 [42, 44–46]. As a result, the values of our simulation predicts reasonable values. In particular, our simulation result is in excellent agreement with $\gamma_e = 1.15 \pm 0.02$ reported in reference [28].

It should be mentioned that the quantitative comparison between our simulation and the experiments in the literature (e.g. reference [28]) is not the main focus in this work because there exist discrepancies between the two scales. We only hope to prove that our scale reduced simulation still captures the most important flow characteristics of MN plasmas. This lays the foundation of our effort to uncover the mechanism of magnetic thrust generation with an emphasis on the role of electron kinetics that was rarely addressed in previous studies.

4. Magnetic thrust generation

As we have seen in figure 3, the applied magnetic field does not necessarily lead to the increment of ion axial velocity. Then, one would ask whether a MN could make positive contribution to thrust. This is a more essential issue to propulsive MNs and the EP community.

The thrust delivered by the plasma is closely related to the change of the total axial flow momentum of plasma. The total axial flow momentum flux τ_{tot} per unit cross section is given as follows [21, 22, 24, 47]

$$\tau_{tot}(z, r) = n_i m_i u_{i,z}^2 + p_e, \tag{5}$$

where the terms on the right-hand side correspond to the ion momentum flux and electron pressure (or electron thermal flux), respectively. $p_e = n_e k_b T_e$ with T_e computed according to equation (4). The differential change of the axial flow momentum of the plasma per unit time can be shown to be

$$\mathrm{d}F_{tot} = \frac{\partial \tau_{tot}}{\partial z} 2\pi r \mathrm{d}r\, \mathrm{d}z. \tag{6}$$

We are interested in the plume plasma, that is, the plasma in the control volume bounded by the source exit plane at $z = 0$, a generic cross section at some axial position $z = z'$ outside the source and the plasma boundary with the radius of $r_p(z)$. The change of the total axial flow momentum of the plume plasma per unit time can be obtained by the volume integration of equation (6) as

$$\begin{aligned}\Delta F_{plume}(z = z') &= \int_0^{r_p(z)} \int_0^{z'} \frac{\partial \tau_{tot}}{\partial z} 2\pi r \mathrm{d}r\, \mathrm{d}z \\ &= F_{tot}(z = z') - F_{tot}(z = 0),\end{aligned} \tag{7}$$

where $F_{tot}(z)$ is the axial momentum carried by the flow through the cross section at z per unit time and reads

$$\begin{aligned}F_{tot}(z) &= \int_0^{r_p(z)} \tau_{tot}(z, r) 2\pi r \mathrm{d}r \\ &\equiv F_i(z) + F_e(z),\end{aligned} \tag{8}$$

with

$$F_i(z) = \int_0^{r_p(z)} n_i m_i u_{i,z}^2 2\pi r \mathrm{d}r, \quad \text{and} \tag{9}$$

$$F_e(z) = \int_0^{r_p(z)} p_e 2\pi r \mathrm{d}r. \tag{10}$$

Without loss of generality, we can replace z' with z in equation (7) for $z \geqslant 0$ and obtain

$$F_{tot}(z) = F_0 + \Delta F_{plume}(z), \tag{11}$$

where $F_0 = F_{tot}(0)$ is the axial momentum carried by the plasma flow into the plume region from the source. $F_{tot}(z)$ is equal to the total axial force acting on all the plasma downstream to z (including the plasma inside the source) according to Newton's 2nd law. It is the sum of the axial force acting on the plasma inside the source equal to F_0 and that acting on the plume plasma equal to $\Delta F_{plume}(z)$. We will not distinguish between the terms axial flow momentum of plasma and axial force acting on the plasma hereafter. It is noted that the nomenclature 'local thrust' is also used, e.g., in reference [21].

By combining the fluid equations for ions and electrons, one can show $\Delta F_{plume}(z)$ can be expressed as [22–24]

$$\Delta F_{plume}(z) = F_B(z) + F_r(z), \tag{12}$$

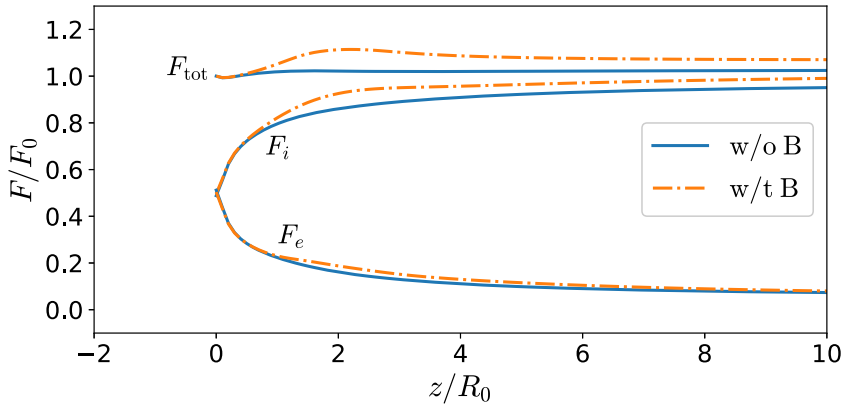

Figure 5. Axial flow momentum of plasma from PIC simulations: a comparison between the cases without and with applied magnetic field.

with

$$F_{\rm B}(z) = \int_0^{r_{\rm p}(z)} \int_0^z -J_\theta B_r 2\pi r {\rm d}r\,{\rm d}z, \quad \text{and} \tag{13}$$

$$\begin{aligned} F_r(z) &= \int_0^{r_{\rm p}(z)} \int_0^z -\frac{\partial}{\partial r}\left(r n_{\rm i} m_{\rm i} u_{{\rm i},r} u_{{\rm i},z}\right) 2\pi {\rm d}r\,{\rm d}z, \\ &= \int_0^z -2\pi \left(r n_{\rm i} m_{\rm i} u_{{\rm i},r} u_{{\rm i},z}\right)_{r=r_{\rm p}(z)} {\rm d}z, \end{aligned} \tag{14}$$

where $F_{\rm B}(z)$ and $F_r(z)$ denote the net increase in the axial momentum of plume plasma due to the volumetric Lorentz force and the plasma-boundary interaction in the radial direction, respectively. To get the final form of $F_r(z)$ shown in equation (14), we have taken the fact that $\left(r n_{\rm i} m_{\rm i} u_{{\rm i},r} u_{{\rm i},z}\right)_{r=0} = 0$. Combining equations (8), (11) and (12), we express the total axial flow momentum of plasma per unit time (or equivalently the total axial force acting on plasma) as

$$\begin{aligned} F_{\rm tot}(z) &\equiv F_{\rm i}(z) + F_{\rm e}(z) \\ &= F_0 + F_{\rm B}(z) + F_r(z). \end{aligned} \tag{15}$$

Figure 5 shows the total axial flow momentum of plasma along with its ion and electron components both without and with the magnetic field. When the magnetic field is absent, $F_{\rm i}$ increases and $F_{\rm e}$ decreases, but the total axial flow momentum is conserved. This process is the geometric expansion which has been investigated extensively [42, 48]. The increase of $F_{\rm i}$ results from the ambipolar acceleration of ions. For geometric expansion, $F_{\rm B}$ in equation (15) is zero; Lafleur *et al* [47] showed that F_r should also vanish as no mechanism can exert force on plasma at the plasma boundary. The total axial flow momentum $F_{\rm tot}$ is therefore conserved in the plume and equals F_0.

Additional thrust may be produced if the divergent magnetic field is applied. Figure 5 also presents our full PIC results of the axial flow momentum in the presence of magnetic field. $F_{\rm tot}$ increases to reach the maximum of about $1.12F_0$ at $z \simeq 2R_0$ and then gradually decreases to a plateaued value of about $1.07F_0$. Both $F_{\rm i}$ and $F_{\rm e}$ are enhanced by the MN effect, but the increase in $F_{\rm i}$ is greater. We note that the increase in the axial flow momentum starts from $z \simeq 0.5R_0$. We can refer to the plane where the flow quantities, e.g. the total axial flow momentum of plasma, reach the plateau as the exit of MN [49, 50]. Then, we can conclude that $1.07F_0$ is the total gain of axial momentum of plasma per unit time, which also equals total axial force acting on the plasma. The thrust delivered by the plasma should be equal in magnitude and opposite in direction to this force. The interaction of the plume plasma with the MN has generated an additional thrust of about $0.07F_0$, which is recognized as the magnetic thrust. It is known that many factors, e.g. the alignment and strength of magnetic field, plasma source, operation condition, etc, can affect the gain of magnetic thrust. The simplified MN model treated in this work has produced a relatively small amount of additional thrust in the MN plume, with only about $7\%F_0$. This suggests much of the momentum transfer to the thruster actually occur upstream of the throat in this specific model and operation condition.

Equation (15) suggests that the potential sources of the additional thrust in the presence of MN include the volumetric contribution $F_{\rm B}$ and the surface (boundary) contribution F_r. Some previous studies [22–24] have considered F_r should also vanish even in the presence of MN by extending the conclusion drawn from the non-MN situation in reference [47] However, Ahedo and Merino [21] postulated a second Lorentz force contribution due to the surface azimuthal current developing at the plasma boundary should exist. If this hypothesis is true, then F_r might be non-zero.

We now examine the source responsible for the additional thrust gain in the plume by our full PIC data. The total azimuthal electric current density J_θ in equation (13) is a sum of ion ($J_{{\rm i},\theta} = e n_{\rm i} u_{{\rm i},\theta}$) and electron ($J_{{\rm e},\theta} = -e n_{\rm e} u_{{\rm e},\theta}$) components. Figure 6 shows the azimuthal electric current densities obtained from our PIC simulation, along with MRFL denoted by the black solid line with a quiver. $J_\theta < 0$ corresponds to the diamagnetic current which produces positive force on plasma while $J_\theta > 0$ means the current is paramagnetic. The diamagnetic current exists mainly in the vicinity of MRFL. In particular, a very strong diamagnetic electric current is observed within a layer of about $10r_{\rm ce}$ thick just outside MRFL for $z \lesssim 2R_0$. The paramagnetic feature is prevalent in the inner region of MRFL, except for the region near MRFL. The ion current is observed to take up less than 1% of the total azimuthal electric current, and thus the electron component is

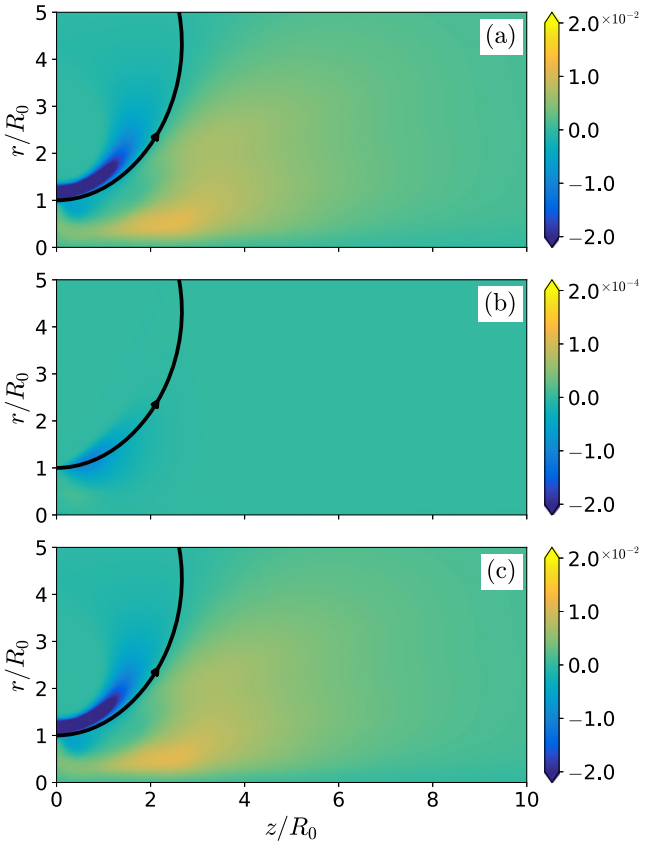

Figure 6. PIC results of azimuthal electric current densities: (a) total current density J_θ, (b) ion component $J_{\mathrm{i},\theta}$ and (c) electron component $J_{\mathrm{e},\theta}$. The results shown are normalized by $en_0v_{\mathrm{te}0}$.

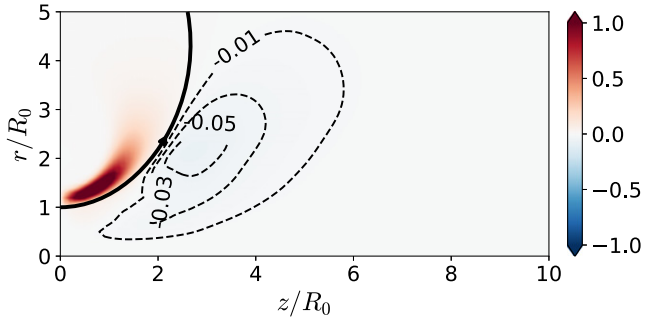

Figure 7. Distribution of surface density of Lorentz force $\tau_{\mathrm{B}} = -J_\theta B_r 2\pi r$. The result is normalized by $n_0k_{\mathrm{b}}T_{\mathrm{e}0}$.

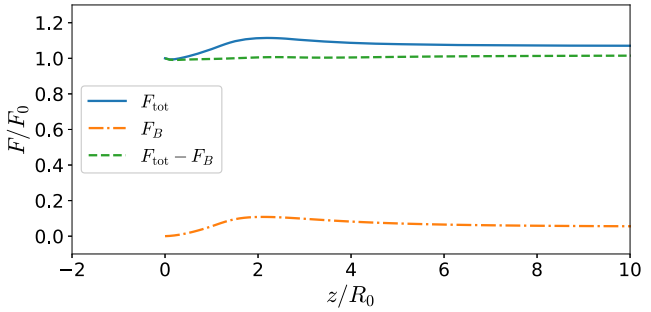

Figure 8. Axial flow momentum of plasma from PIC simulation with applied magnetic field: role of Lorentz force.

dominant ($J_\theta \simeq J_{\mathrm{e},\theta}$). The negligible role of ion component in accounting for the azimuthal electric current is also validated by experiments [25]. Nevertheless, it is interesting to see a diamagnetic feature of the ion plasma component.

The integrand $-J_\theta B_r 2\pi r$ in equation (13) can be considered as the 'surface density' of Lorentz force, which is denoted as τ_{B} hereafter. Figure 7 shows the dimensionless surface density of Lorentz force τ_{B}. τ_{B} is almost zero near the throat just outside MRFL because B_r is negligible even though J_θ is maximum there. Along the magnetic field line, τ_{B} changes non-monotonically and achieves the maximum value at $z \simeq R_0$. A large area inside MRFL is occupied by slightly negative τ_{B} due to the paramagnetic effects, as shown by the dashed lines. Though the absolute value of τ_{B} in this region is small, its integral effect cannot be neglected as we have seen the decrease of F_{tot} for $z \gtrsim 2R_0$.

F_{B} can easily be evaluated via a numerical integration once τ_{B} is known. Figure 8 shows F_{tot}, F_{B} and their difference evaluated based on our PIC results. It is clear that $F_{\mathrm{tot}} - F_{\mathrm{B}}$ does not change with z and equals the source thrust. This supports the conclusion that F_r also vanishes even in the presence of MN. The volumetric Lorentz force is the only source for the additional thrust gain from the interaction of the plume plasma with the MN.

Finally, it is worth mentioning that the increase in total ion momentum F_{i} can be much larger than the additional thrust gain in the MN, as shown in figure 5. In the MN, the decrease in electron pressure due to plasma expansion can account for the major contribution to the ion acceleration. This is in contrast to the process of ion acceleration in Hall thrusters, where the change of electron pressure due to plasma expansion is negligible and the increase in total ion momentum equals the thrust [51]. With that said, the increase in momentum of the ions that occurs electrostatically in the MN is not equivalent to the Lorentz force acting on the thruster (the magnetic thrust). Figure 5 also suggests that one may not be able to equate the axial ion flow momentum to the total thrust of the MN equipped thrusters as the electron pressure contribution is not negligible. In other words, $n_{\mathrm{i}}m_{\mathrm{i}}u_{\mathrm{i}}^2/n_{\mathrm{e}}k_{\mathrm{b}}T_{\mathrm{e}} = M^2$ is not much less than 1, where the quasi-neutral assumption ($n_{\mathrm{i}} = n_{\mathrm{e}}$) has been made. This is in contrast to the gridded ion thrusters or Hall thrusters for which M at the thruster exit is at least 10 and thereby one can consider the total thrust equal to the ion momentum.

5. Transport of collisionless magnetized electrons

The correct assessment of the magnetic thrust requires evaluating the azimuthal current accurately. This is one of the most essential tasks in the fluid modeling of MN plasma flows.

As the ion component has been demonstrated to have negligible contribution to the magnetic thrust, we consider only the electron fluid here. For collisionless electrons, the full fluid

momentum equation is written as

$$\frac{\partial}{\partial t}\left(m_{\mathrm{e}} n_{\mathrm{e}} \mathbf{u}_{\mathrm{e}}\right)+\nabla \cdot\left(m_{\mathrm{e}} n_{\mathrm{e}} \mathbf{u}_{\mathrm{e}} \mathbf{u}_{\mathrm{e}}\right) = -\nabla p_{\mathrm{e}}-e n_{\mathrm{e}}\left(\mathbf{E}+\mathbf{u}_{\mathrm{e}} \times \mathbf{B}\right)+\nabla \cdot \pi_{\mathbf{e}}, \tag{16}$$

where $\mathbf{u}_{\mathrm{e}}=\left(u_{\mathrm{e},r}, u_{\mathrm{e},z}, u_{\mathrm{e},\theta}\right)$ is the bulk velocity vector of electron, and $\pi_{\mathbf{e}}$ is the stress tensor due to thermal motion of electron particles. According to the kinetic theory, $\pi_{\mathbf{e}}$ is defined as

$$\pi_{\mathbf{e}} \equiv p_{\mathrm{e}} \mathbf{I}-\left[\int m_{\mathrm{e}}\left(\mathbf{v}-\mathbf{u}_{\mathrm{e}}\right)\left(\mathbf{v}-\mathbf{u}_{\mathrm{e}}\right) f_{\mathrm{e}}(\mathbf{x}, \mathbf{v}) \mathrm{d}^{3} \mathbf{v}\right], \tag{17}$$

where $\mathbf{I}$ is the identity matrix and $p_{\mathrm{e}}=n_{\mathrm{e}} k_{\mathrm{b}} T_{\mathrm{e}}$ is the electron pressure. In our steady axisymmetric flow ($\partial/\partial t=0$ and $\partial/\partial\theta=0$), we can write the radial (r-) and axial (z-) components of equation (16) in cylindrical coordinates (r, z, θ) as

$$\frac{\partial M_{\mathrm{e},rr}}{\partial r}+\frac{\partial M_{\mathrm{e},rz}}{\partial z}+\frac{M_{\mathrm{e},rr}-M_{\mathrm{e},\theta\theta}}{r} = -\frac{\partial p_{\mathrm{e}}}{\partial r}-e n_{\mathrm{e}}\left(E_{r}+u_{\mathrm{e},\theta} B_{z}\right) + \frac{\partial \pi_{\mathrm{e},rr}}{\partial r}+\frac{\partial \pi_{\mathrm{e},rz}}{\partial z}+\frac{\pi_{\mathrm{e},rr}}{-}\pi_{\mathrm{e},}{}_{\theta\theta r}, \tag{18}$$

$$\frac{\partial M_{\mathrm{e},zz}}{\partial z}+\frac{\partial M_{\mathrm{e},rz}}{\partial r}+\frac{M_{\mathrm{e},rz}}{r} = -\frac{\partial p_{\mathrm{e}}}{\partial z}-e n_{\mathrm{e}}\left(E_{z}-u_{\mathrm{e},\theta} B_{r}\right) + \frac{\partial \pi_{\mathrm{e},zz}}{\partial z}+\frac{\partial \pi_{\mathrm{e},rz}}{\partial r}+\frac{\pi_{\mathrm{e},rz}}{r}, \tag{19}$$

where $\pi_{\mathrm{e},jk}$ indicates the 'jk' component of the stress tensor defined in equation (17), $M_{\mathrm{e},jk}=m_{\mathrm{e}} n_{\mathrm{e}} u_{\mathrm{e},j} u_{\mathrm{e},k}$; the indices '$j$' and '$k$' in the subscripts of M_{e} and π_{e} can be r, z or θ. We can write the azimuthal electron current density ($J_{\mathrm{e},\theta}=-e n_{\mathrm{e}} u_{\mathrm{e},\theta}$) as

$$J_{\mathrm{e},\theta}=e n_{\mathrm{e}} \frac{E_{r}}{B_{z}}+\frac{1}{B_{z}} \frac{\partial p_{\mathrm{e}}}{\partial r} + \frac{1}{B_{z}}\left(\frac{\partial M_{\mathrm{e},rr}}{\partial r}+\frac{\partial M_{\mathrm{e},rz}}{\partial z}+\frac{M_{\mathrm{e},rr}-M_{\mathrm{e},\theta\theta}}{r}\right) - \frac{1}{B_{z}}\left(\frac{\partial \pi_{\mathrm{e},rr}}{\partial r}+\frac{\partial \pi_{\mathrm{e},rz}}{\partial z}+\frac{\pi_{\mathrm{e},rr}-\pi_{\mathrm{e},\theta\theta}}{r}\right), \tag{20}$$

or

$$J_{\mathrm{e},\theta}=-e n_{\mathrm{e}} \frac{E_{z}}{B_{r}}-\frac{1}{B_{r}} \frac{\partial p_{\mathrm{e}}}{\partial z} - \frac{1}{B_{r}}\left(\frac{\partial M_{\mathrm{e},zz}}{\partial z}+\frac{\partial M_{\mathrm{e},rz}}{\partial r}+\frac{M_{\mathrm{e},rz}}{r}\right) + \frac{1}{B_{r}}\left(\frac{\partial \pi_{\mathrm{e},zz}}{\partial z}+\frac{\partial \pi_{\mathrm{e},rz}}{\partial r}+\frac{\pi_{\mathrm{e},rz}}{r}\right), \tag{21}$$

depending on either equation (18) or (19) is used. In equations (20) and (21), the terms on the right-hand side correspond to the contributions due to the $\mathbf{E} \times \mathbf{B}$, diamagnetic, inertial and stress effects, respectively.

We note that the inertial and stress terms were ignored in most previous fluid-based MN plasma analyses [21–25],

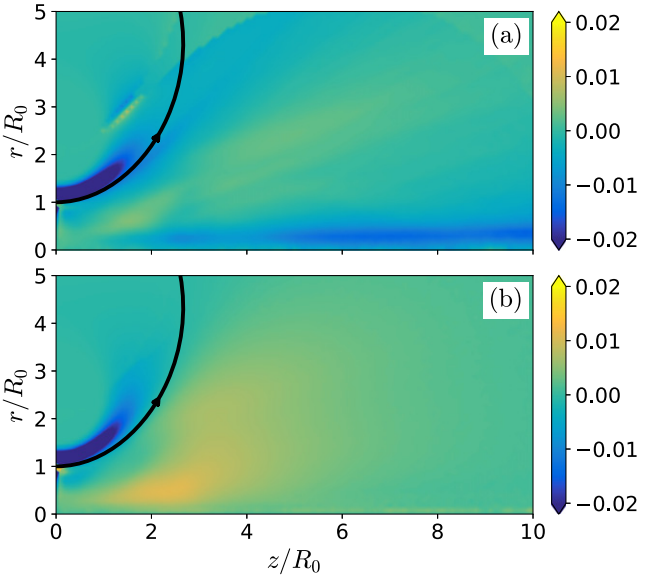

Figure 9. 2D contours of fluid-based azimuthal electron current density: (a) simplified fluid model and (b) full fluid momentum equation. The results are normalized by $en_0v_{\mathrm{te}0}$.

resulting in the following expressions based on the simplified massless ideal fluid model,

$$J_{\mathrm{e},\theta}=e n_{\mathrm{e}} \frac{E_{r}}{B_{z}}+\frac{1}{B_{z}} \frac{\partial p_{\mathrm{e}}}{\partial r}, \tag{22}$$

or

$$J_{\mathrm{e},\theta}=-e n_{\mathrm{e}} \frac{E_{z}}{B_{r}}-\frac{1}{B_{r}} \frac{\partial p_{\mathrm{e}}}{\partial z}. \tag{23}$$

In principle, the calculation of $J_{\mathrm{e},\theta}$ should be independent of which component of the momentum equation to be used. In other words, equations (22) and (23) should yield the same value of $J_{\mathrm{e},\theta}$ if the inertial and stress contributions are negligible. The choice of which equation to calculate $J_{\mathrm{e},\theta}$ in practice is purely for convenience, and equation (22) was usually adopted [22–25]. When computing $J_{\mathrm{e},\theta}$ based on the PIC results, the numerical noise inherent in the particle simulation could be unphysically amplified by $B_z \simeq 0$ if equation (22) is used or by $B_r \simeq 0$ if equation (23) is used. To avoid this trouble, we have taken a mixed rule to evaluate $J_{\mathrm{e},\theta}$, in which the r-component based equation [e.g. equation (22)] is used if $|\tilde{B}_z| < 0.005$ and the z-component one [e.g. equation (23)] is used otherwise.

Figure 9(a) shows $J_{\mathrm{e},\theta}$ based on the simplified fluid model. The result is apparently different from the PIC result given in figure 6(c). Such a difference suggests that the widely used fluid model with only $\mathbf{E} \times \mathbf{B}$ and diamagnetic terms is invalid. The PIC result exhibits a large area with considerable paramagnetic electron current ($J_{\mathrm{e},\theta} > 0$) inside MRFL while the simplified fluid model predicts a much smaller paramagnetic region. Furthermore, the result based on the simplified fluid model shows notable diamagnetic electron current in the region approximately bounded by $z > 2R_0$ and $r < 0.5R_0$, but the PIC result does not.

To identify what leads to the failure of the simplified fluid model, we first assess $J_{\mathrm{e},\theta}$ with the full fluid momentum

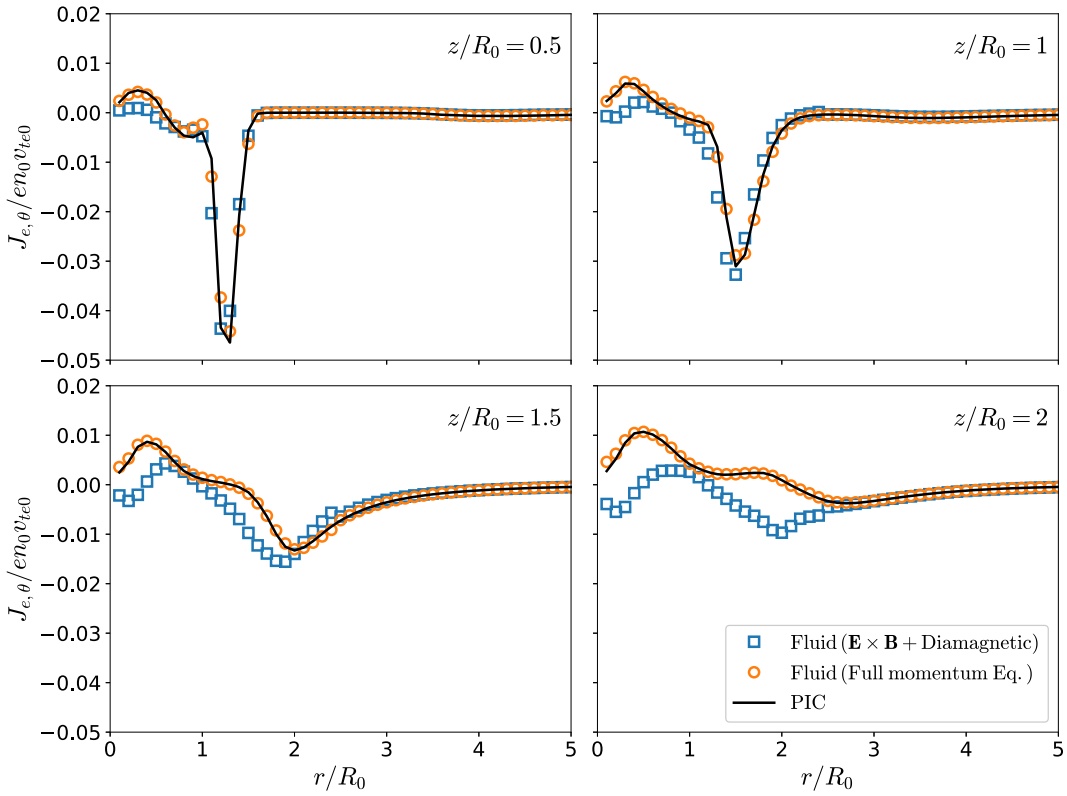

Figure 10. Distribution of $J_{e,\theta}$ versus r: comparison between kinetic and fluid results.

equation in which the inertial and stress terms calculated from the distribution functions in the PIC simulation are included. Figure 9(b) shows the 2D distribution of $J_{e,\theta}$ evaluated based on the full fluid equation. This agrees with the direct PIC result shown in figure 6(c), as it should be. The agreement could be visualized more clearly by the 1D profiles of $J_{e,\theta}$ predicted by various methods along the r-direction for several selected z coordinates, as shown in figure 10. It is interesting to note that the values of $J_{e,\theta}$ (PIC or full fluid momentum equation) minus $J_{e,\theta}$ (simplified fluid model) are generally non-negative, suggesting an underestimate of the 'paramagnetic' effects by the simplified fluid model. This is consistent with the experimental work by Takahashi *et al* [22, 25], in which $J_{e,\theta}$ computed using equation (22) was less 'paramagnetic' than the measured current [25] and the calculated forces arising from magnetic field were larger than or close to the measured values in general [22].

We further examine the individual contribution to the azimuthal electron current from different terms in the full fluid equation. Figure 11 presents the 1D profiles of $J_{e,\theta}$ produced by the $\mathbf{E}\times\mathbf{B}$ plus diamagnetic, the inertial and the stress terms as well as the PIC results for comparison. The 1D profiles are extracted along the same locations as those in figure 10. It can be seen from figure 11 that the current due to inertial effects is almost zero. This is not surprising because the electron mass is too small and the bulk velocity of electrons is also small (same as ion velocity due to ambipolarity) compared to its thermal velocity. The magnitude of the stress induced azimuthal current is of the same order as the $\mathbf{E}\times\mathbf{B}$ and diamagnetic current. The stress is observed to result in a paramagnetic azimuthal current in most area. It is the missing of stress term that causes the failure of the simplified fluid model widely adopted in previous studies. Finally, the excellent agreement between the full fluid and the PIC result as well as the identification of the stress' contribution to the azimuthal current demonstrates that the fluid theory works for collisionless plasma flows, as long as the effects of stress tensor or anisotropy have been properly taken into account.

It should be mentioned that the difference in length scale between simulations and experiments might have quantitative effects on the stress tensor discussed in this section. A parametric investigation into the potential effects of length scale on the stress tensor and subsequently on the azimuthal current and magnetic thrust production will be a future work.

We also note that the electron transport associated with the stress tensor may not be the only source contributing negatively to the magnetic thrust. A recent experiment shows the presence of azimuthal instabilities could also enhance the electron transport, resulting in a lower thrust [52]. Therefore, it is likely that in the MN plume, multiple mechanisms coexist to enhance the electron transport which is not captured by the ideal fluid model. The investigations into the importance of individual mechanisms require further high-fidelity larger scale 3D simulations or experiments with sophisticated measurement techniques.

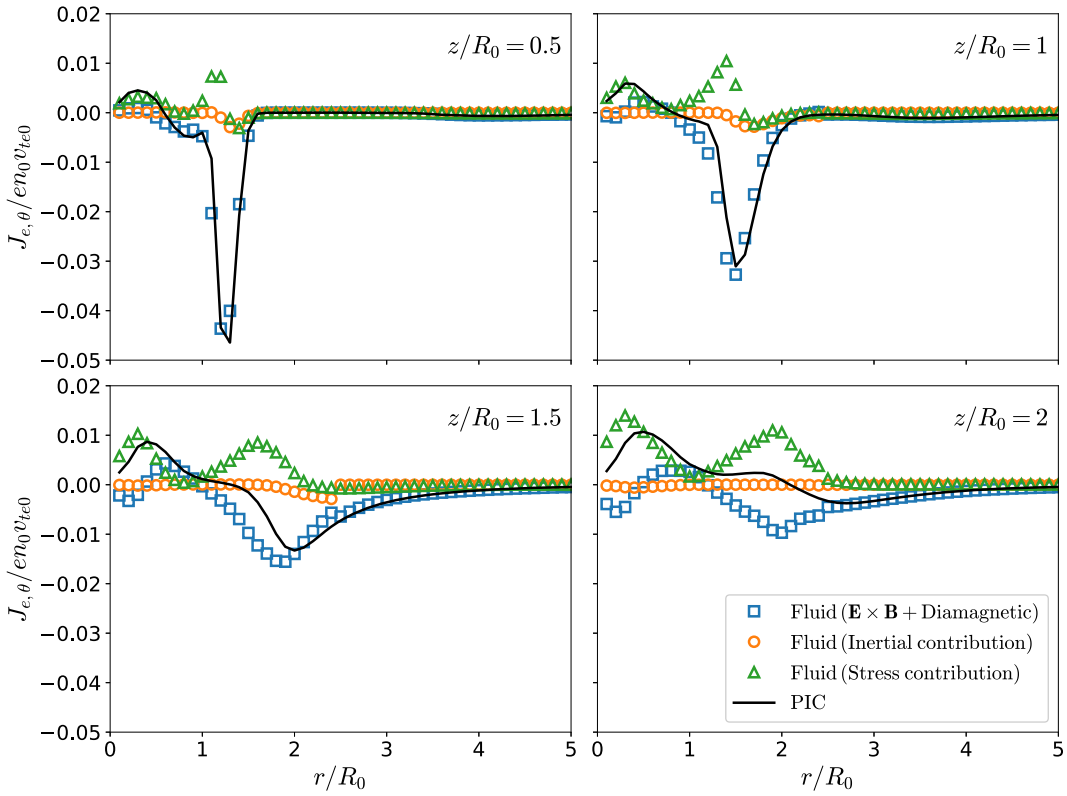

Figure 11. Distribution of $J_{e,\theta}$ versus r: contributions from different components of fluid results.

6. Conclusions

We take advantage of an axisymmetric full PIC model to simulate the expansion of plasma plume in an MN. The representative physical quantities in the plume obtained from our simulation show good agreements with the data from the experiment operating under a similar condition. The simulation results in the absence and presence of an MN are compared directly. The comparison shows that the thrust in the plume can be increased, by about 10%, while the on-axis ion acceleration is reduced if the magnetic field is applied. This demonstrates the necessity of taking the 2D effects into account if there is a focus on the propulsive performance of MN. The acceleration of ions in the plume results from two parts, the volumetric Lorentz force due to the interaction of the plasma with the MN and the electron pressure decrease due to plasma expansion. The latter one can be the dominant contribution to the ion acceleration in the MN, but does not increase the thrust. The enhanced (magnetic) thrust is completely attributed to the volumetric Lorentz force. The fully kinetic result manifests the deficiency of the simplified fluid model widely adopted to evaluate the electron azimuthal current in the literature. It is found that the role of electron transport, in connection with the stress tensor terms, is as important as the $\mathbf{E}\times\mathbf{B}$ and diamagnetic drift effects and must be included in fluid modeling. The full PIC simulation reveals that the electron transport effects tend to induce a paramagnetic current and thus undermine the thrust enhancement in MN, supported by the experiment clues.

It is worth mentioning again that the fraction of magnetic thrust to the total thrust depends on various factors, such as the alignment and strength of magnetic field, plasma source, operation condition, etc. As a result, the reported magnetic thrusts vary in a huge range, about 10% to 60% of the total thrust [38, 53]. Moreover, it is possible that an applied magnetic field could even contribute negatively to the propulsive performance if it is improperly operated. The value of F_B/F_0 obtained by our simulation is within the reasonable range of the reported values. We want to point out that the main focus of this work is to identify the source of magnetic thrust and to uncover the importance of the electron transport process ignored by most previous studies. Comprehensive investigations on the factors that affect and/or maximize the propulsive performance of thrusters by the fully kinetic method considering 2D and 3D effects will be carried out in the future.

Acknowledgments

YH and ZH were partially supported by the LHD Youth Innovation Fund from the State Key Laboratory of High Temperature Gas Dynamics (Grant No. LHD2019CX12). YC was supported by Shenzhen Technology Projects (No. ZDSYS201707280904031). QS was supported by the Strategic Priority Research Program of the Chinese Academy of Sciences (Grant No. XDA17030100). YH would also like to thank Mr. Chen Cui from University of Southern California and Dr. Jianwu He from National Microgravity Laboratory of Chinese Academy of Sciences for helpful discussions

on non-classical electron transport and thrust diagnostics, respectively.

Data availability statement

The data that support the findings of this study are available upon reasonable request from the authors.

ORCID iDs

Yuan Hu https://orcid.org/0000-0001-6870-183X

References

[1] Andersen S A, Jensen V O, Nielsen P and D'Angelo N 1968 *Phys. Lett.* A **27** 527–8
[2] Andersen S A, Jensen V O, Nielsen P and D'Angelo N 1969 *Phys. Fluids* **12** 557–60
[3] Charles C 2009 *J. Phys. D: Appl. Phys.* **42** 163001
[4] Takahashi K 2019 *Rev. Mod. Plasma Phys.* **3** 3
[5] Kaganovich I D *et al* 2020 *Phys. Plasmas* **27** 120601
[6] Cannat F, Lafleur T, Jarrige J, Chabert P, Elias P-Q and Packan D 2015 *Phys. Plasmas* **22** 053503
[7] Correyero S, Jarrige J, Packan D and Ahedo E 2019 *Plasma Sources Sci. Technol.* **28** 095004
[8] Krülle G, Auweter-Kurtz M and Sasoh A 1998 *J. Propul. Power* **14** 754–63
[9] Arefiev A V and Breizman B N 2004 *Phys. Plasmas* **11** 2942–9
[10] Olsen C *et al* 2015 *IEEE Trans. Plasma Sci.* **43** 252–68
[11] Arefiev A V and Breizman B N 2008 *Phys. Plasmas* **15** 042109
[12] Arefiev A V and Breizman B N 2009 *Phys. Plasmas* **16** 055707
[13] Longmier B W *et al* 2011 *Plasma Sources Sci. Technol.* **20** 015007
[14] Charles C and Boswell R 2003 *Appl. Phys. Lett.* **82** 1356–8
[15] Charles C 2010 *Appl. Phys. Lett.* **96** 051502
[16] Baalrud S D, Lafleur T, Boswell R W and Charles C 2011 *Phys. Plasmas* **18** 063502
[17] Rao S and Singh N 2012 *Phys. Plasmas* **19** 093507
[18] Ahedo E 2011 *Phys. Plasmas* **18** 033510
[19] Fruchtman A 2006 *Phys. Rev. Lett.* **96** 065002
[20] Merino M and Ahedo E 2013 *Phys. Plasmas* **20** 023502
[21] Ahedo E and Merino M 2010 *Phys. Plasmas* **17** 073501
[22] Takahashi K, Lafleur T, Charles C, Alexander P and Boswell R W 2011 *Phys. Rev. Lett.* **107** 235001
[23] Fruchtman A, Takahashi K, Charles C and Boswell R W 2012 *Phys. Plasmas* **19** 033507
[24] Takahashi K, Lafleur T, Charles C, Alexander P and Boswell R W 2012 *Phys. Plasmas* **19** 083509
[25] Takahashi K, Chiba A, Komuro A and Ando A 2016 *Plasma Sources Sci. Technol.* **25** 055011
[26] Merino M and Ahedo E 2015 *IEEE Trans. Plasma Sci.* **43** 244–51
[27] Zhang Y, Charles C and Boswell R 2016 *Phys. Rev. Lett.* **116** 025001
[28] Little J M and Choueiri E Y 2016 *Phys. Rev. Lett.* **117** 225003
[29] Takahashi K, Charles C, Boswell R and Ando A 2018 *Phys. Rev. Lett.* **120** 045001
[30] Kim J Y, Chung K S, Kim S, Ryu J H, Chung K-J and Hwang Y S 2018 *New J. Phys.* **20** 063033
[31] Kim J Y, Jang J Y, Chung K S, Chung K-J and Hwang Y S 2019 *Plasma Sources Sci. Technol.* **28** 07LT01
[32] Martinez-Sanchez M, Navarro-Cavallé J and Ahedo E 2015 *Phys. Plasmas* **22** 053501
[33] Ahedo E, Correyero S, Navarro-Cavallé J and Merino M 2020 *Plasma Sources Sci. Technol.* **29** 045017
[34] Ramos J J 2003 *Phys. Plasmas* **10** 3601–7
[35] Kaganovich I D, Demidov V I, Adams S F and Raitses Y 2009 *Plasma Phys. Control. Fusion* **51** 124003
[36] Boswell R, Takahashi K, Charles C and Kaganovich I 2015 *Front. Phys.* **3** 14
[37] Singh N, Rao S and Ranganath P 2013 *Phys. Plasmas* **20** 032111
[38] Chen Z, Wang Y, Tang H, Ren J, Li M, Zhang Z, Cao S and Cao J 2020 *Phys. Rev.* E **101** 053208
[39] Little J M and Choueiri E Y 2019 *Phys. Rev. Lett.* **123** 145001
[40] Geng J, Chen Y, Sun S, Huang W and Wang H 2020 *Plasma Sci. Technol.* **22** 094012
[41] Alexander B, Christine C and Boswell R 2018 *J. Phys. D: Appl. Phys.* **51** 375204
[42] Hu Y, Wang J and Sun Q 2020 *Plasma Sources Sci. Technol.* **29** 125004
[43] Hu Y and Wang J 2018 *Phys. Rev.* E **98** 023204
[44] Li M, Merino M, Ahedo E and Tang H 2019 *Plasma Sources Sci. Technol.* **28** 034004
[45] Dannenmayer K and Mazouffre S 2013 *Plasma Sources Sci. Technol.* **22** 035004
[46] Merino M, Fajardo P, Giono G, Ivchenko N, Gudmundsson J-T, Mazouffre S, Loubère D and Dannenmayer K 2020 *Plasma Sources Sci. Technol.* **29** 035029
[47] Lafleur T, Takahashi K, Charles C and Boswell R W 2011 *Phys. Plasmas* **18** 080701
[48] Corr C S, Zanger J, Boswell R W and Charles C 2007 *Appl. Phys. Lett.* **91** 241501
[49] Collard T A and Jorns B A 2019 *Plasma Sources Sci. Technol.* **28** 105019
[50] Wachs B and Jorns B 2020 *Plasma Sources Sci. Technol.* **20** 045002
[51] Goebel D M and Katz I 2008 *Fundamentals of Electric Propulsion: Ion and Hall Thrusters* (New York: Wiley)
[52] Hepner S, Wachs B and Jorns B 2020 *Appl. Phys. Lett.* **116** 263502
[53] Sánchez-Villar Á, Zhou J, Ahedo E and Merino M 2021 *Plasma Sources Sci. Technol.* **30** 045005